HHS Public Access

Author manuscript

Nat Cell Biol. Author manuscript; available in PMC 2020 July 11.

Published in final edited form as:

Nat Cell Biol. 2019 November ; 21(11): 1403–1412. doi:10.1038/s41556-019-0404-4.

Tumour exosomal CEMIP protein promotes cancer cell colonization in brain metastasis

Gonçalo Rodrigues[1,2], **Ayuko Hoshino**[1,3,4], **Candia M. Kenific**[1], **Irina R. Matei**[1], **Loïc Steiner**[1,5], **Daniela Freitas**[1,6,7,8], **Han Sang Kim**[1,9], **Peter R. Oxley**[10], **Ilana Scandariato**[1], **Irene Casanova-Salas**[1], **Jinxiang Dai**[11], **Chaitanya R. Badwe**[12], **Brunilde Gril**[13], **Milica Tešić Mark**[14], **Brian D. Dill**[14], **Henrik Molina**[14], **Haiying Zhang**[1], **Alberto Benito-Martin**[1], **Linda Bojmar**[1], **Yonathan Ararso**[1], **Katharine Offer**[1], **Quincey LaPlant**[1], **Weston Buehring**[1], **Huajuan Wang**[1], **Xinran Jiang**[1], **Tyler M. Lu**[12,15], **Yuan Liu**[16], **Joshua K. Sabari**[17], **Sandra J. Shin**[18], **Navneet Narula**[18], **Paula S. Ginter**[18], **Vinagolu K. Rajasekhar**[19], **John H. Healey**[20], **Etienne Meylan**[5], **Bruno Costa-Silva**[21], **Shizhen Emily Wang**[22], **Shahin Rafii**[12], **Nasser Khaled Altorki**[23], **Charles M. Rudin**[17], **David R. Jones**[16], **Patricia S. Steeg**[13], **Héctor Peinado**[1,24], **Cyrus M. Ghajar**[11], **Jacqueline Bromberg**[25,26], **Maria de Sousa**[1,2], **David Pisapia**[18], **David Lyden**[1]

[1]Children's Cancer and Blood Foundation Laboratories, Departments of Pediatrics, and Cell and Developmental Biology, Drukier Institute for Children's Health, Meyer Cancer Center, Weill Cornell Medicine, New York, New York 10021, USA [2]Graduate Program in Areas of Basic and Applied Biology, Abel Salazar Biomedical Sciences Institute, University of Porto, 4050-313, Portugal [3]International Research Center for Neurointelligence (WPI-IRCN), The University of Tokyo, Tokyo, Japan [4]JST, PRESTO [5]Swiss Institute for Experimental Cancer Research, School of Life Sciences, Ecole Polytechnique Fédérale de Lausanne, 1015 Lausanne, Switzerland [6]i3S-Institute

Correspondence and requests for materials should be addressed to M.D.S. (mdesousa@ibmc.up.pt), D.P. (djp2002@med.cornell.edu), and D.L. (dcl2001@med.cornell.edu).

AUTHOR CONTRIBUTIONS

G.R. designed the experimental approach, performed the experimental work, analyzed the data, coordinated the project and wrote the manuscript. A.H. performed primary tumour growth and exosome education *in vivo* studies, cancer cell proliferation *in vitro* studies, cancer cell culture and exosome isolation, coordinated the project and wrote the manuscript. C.M.K. generated CEMIP overexpression, performed molecular cloning work and genetic manipulation of cancer cells, cancer cell culture and exosome isolation, coordinated the project and wrote the manuscript. I.R.M. performed brain slice *ex vivo* FACS analysis and exosome education *in vivo* studies, cancer cell culture and exosome isolation, coordinated the project, wrote and reviewed the manuscript. L.S. performed brain slice *ex vivo* experimental work, tissue processing and immunostaining, *ex vivo* and *in vivo* ImageJ data analysis and quantification, cancer cell invasion *in vitro* studies, western blot analysis, cancer cell culture and exosome isolation, and contributed to figure panel assembly. D.F. performed density gradient exosome isolation, characterization and analysis, western blot analysis, and cancer cell culture. H.S.K. and P.R.O. performed RNA sequencing data analysis. I.S. performed tissue processing and immunostaining, *ex vivo* and *in vivo* ImageJ data analysis and quantification, cancer cell culture and exosome isolation. I.C.S. performed western blot analysis and assisted in analysis of human data. J.D., C.R.B., and T.M.L. performed *in vitro* brain endothelial cell experimental work and FACS analysis. M.T.M., B.D.D., and H.M. performed exosome mass spectrometry and proteomic data analysis. A.B.M. assisted in mouse studies and FACS analysis. H.W. and X.J. assisted in tissue processing and immunostaining, cancer cell culture and exosome isolation. L.B., K.O., Q.L., Y.A., W.B. and H.W. received and processed human samples. Y.A., W.B. and H.W. assisted in the maintenance of mouse colonies. Y.L., J.K.S., S.J.S., N.N., J.H.H., N.K.A., C.M.R., D.R.J. and D.P. provided human samples. V.K.R. generated and provided the N2LA human lung cancer cell line. S.E.W. provided the 231-HM human breast cancer cell line. B.G. and P.S.S. provided the 231BR human breast cancer cell line and gave feedback on the project. S.R. provided endothelial cell expertise and reagents. D.P. coordinated human studies and contributed to the experimental design. D.P., N.N., and P.S.G. analyzed the human data. E.M. and H.Z. read the manuscript and gave feedback on the project. B.C.S., H.P., C.M.G. and J.B. contributed to hypothesis discussion, experimental design, data interpretation and project coordination. M.D.S. coordinated the project, contributed to hypothesis discussion, experimental design, data interpretation and wrote the manuscript. D.L. conceived the hypothesis, led the project, interpreted the data and wrote the manuscript.

The authors declare no competing financial interests.

for Research and Innovation in Health, University of Porto, Rua Alfredo Allen 208, Porto 4200-135, Portugal [7]IPATIMUP -Institute of Molecular Pathology and Immunology of the University of Porto, Rua Dr. Roberto Frias s/n, Porto 4200-465, Portugal [8]Instituto de Ciências Biomédicas Abel Salazar (ICBAS), University of Porto, Rua de Jorge Viterbo Ferreira n.228, Porto 4050-313, Portugal [9]Yonsei Cancer Center, Division of Medical Oncology, Departments of Internal Medicine, and Pharmacology, Yonsei University College of Medicine, Seoul 03722, Korea [10]Samuel J. Wood Library, Weill Cornell Medicine, 1300 York Avenue, New York, NY 10065, USA [11]Public Health Sciences Division/Translational Research Program, Fred Hutchinson Cancer Research Center, Seattle, Washington 98109, USA [12]Ansary Stem Cell Institute, Division of Regenerative Medicine, Department of Medicine, Weill Cornell Medicine, New York, New York 10065, USA [13]Woman's Malignancies Branch, Center for Cancer Research, National Cancer Institute, Bethesda, MD 20892, USA [14]Proteomics Resource Center, The Rockefeller University, 1230 York Avenue, New York, NY, 10065-6399, USA [15]Ronald O. Perelman and Claudia Cohen Center for Reproductive Medicine and Infertility, Weill Cornell Medicine (WCM), New York, NY, USA [16]Memorial Sloan Kettering Cancer Center, Department of Surgery, New York, NY 10065, USA [17]Memorial Sloan Kettering Cancer Center, Thoracic Oncology Service, New York, NY 10065, USA [18]Department of Pathology and Laboratory Medicine, Weill Cornell Medicine, New York, New York, 10065, USA [19]Breast Medicine Service, Department of Medicine, Memorial Sloan Kettering Cancer Center, New York, New York 10065, USA [20]Orthopaedic Service, Department of Surgery, Memorial Sloan Kettering Cancer Center, 1275 York Avenue, New York, NY 10065 [21]Systems Oncology Group, Champalimaud Research, Champalimaud Centre for the Unknown, Avenida Brasília, Doca de Pedrouços, 1400-038 Lisbon, Portugal [22]Department of Pathology, University of California, San Diego; La Jolla, California, USA [23]Department of Cardiothoracic Surgery, Weill Cornell Medicine, New York, New York, 10065, USA [24]Microenvironment and Metastasis Laboratory, Department of Molecular Oncology, Spanish National Cancer Research Center (CNIO), Madrid 28029, Spain [25]Department of Medicine, Memorial Sloan Kettering Cancer Center, New York, New York 10065, USA [26]Department of Medicine, Weill Cornell Medicine, New York, NY, USA

Abstract

Development of effective therapies against brain metastasis is currently hindered by limitations in our understanding of the molecular mechanisms driving it. Here we define the contributions of tumour-secreted exosomes to brain metastatic colonization and demonstrate that pre-conditioning the brain microenvironment with exosomes from brain metastatic cells enhances cancer cell outgrowth. Proteomic analysis identified cell migration-inducing and hyaluronan-binding protein (CEMIP) as elevated in exosomes from brain metastatic, but not lung or bone metastatic cells. CEMIP depletion in tumour cells impaired brain metastasis, disrupting invasion and tumour cell association with the brain vasculature, phenotypes rescued by pre-conditioning the brain microenvironment with CEMIP$^+$ exosomes. Moreover, uptake of CEMIP$^+$ exosomes by brain endothelial and microglial cells induced endothelial cell branching and inflammation in the perivascular niche by upregulating *Ptgs2*, *Tnf*, and *Ccl/Cxcl* cytokines, known to promote brain vascular remodeling and metastasis. CEMIP was elevated in tumour tissues and exosomes from patients with brain metastasis and predicted brain metastasis progression and patient survival.

Collectively, our findings suggest that targeting of exosomal CEMIP could constitute a future avenue for the prevention and treatment of brain metastasis.

Keywords

Brain metastasis; CEMIP; KIAA1199; tumour exosomes; brain microenvironment; pre-metastatic niche

INTRODUCTION

Despite advances in understanding the molecular determinants that drive metastasis[1], metastatic entry and adaptation to specific organs, particularly the brain, remain poorly understood. The incidence of brain metastasis (BrM) is ten-fold higher than all primary brain tumours combined[2]. Brain metastases most commonly arise from lung and breast cancer, have poor prognosis and high mortality, and lack effective therapy[3]. Hence, identifying tumour-intrinsic properties and/or drivers of the crosstalk between tumour cells and the brain microenvironment that can be targeted to prevent and/or treat BrM is critical.

The brain microenvironment is a hostile “soil” for disseminating tumour cells, resulting in a low metastatic efficiency[4]. Thus, the ability of tumour cells to remodel the brain niche to support survival and outgrowth ultimately determines successful metastatic colonization[5–7]. Among tumour-secreted factors, tumour-derived exosomes are crucial players in cell-to-cell communication[8] that reshape distant microenvironments, such as pre-metastatic niches[9], driving organ-specific metastasis[10–12].

Therefore, we investigated the role of tumour-derived exosomes in remodeling the brain microenvironment during metastatic colonization. We show that cell migration-inducing and hyaluronan-binding protein (CEMIP, KIAA1199), a Wnt-related protein, enriched in brain metastatic breast and lung tumour-derived exosomes, promotes BrM by generating a pro-metastatic environment. Mechanistically, exosomal CEMIP induced a pro-inflammatory vascular niche by upregulating cytokines and chemokines known to promote BrM. CEMIP was identified in exosomes secreted by viable brain metastatic tissues from breast and lung cancer patients. Moreover, high CEMIP expression in human primary and metastatic tumour tissues significantly associated with accelerated BrM progression and poorer survival. Our work provides insight into the molecular mechanisms through which tumour-secreted CEMIP$^+$ exosomes alter the brain’s vascular niche to promote BrM.

RESULTS

Tumour exosome remodeling of the brain microenvironment fosters metastasis

To overcome hurdles in BrM research posed by limitations of the current pre-clinical models[13] and define the specific contribution of tumour-derived exosomes to brain metastatic colonization, we optimized an *ex vivo* organotypic brain slice culture system (Supplementary Fig. 1a)[14]. We pre-treated brain slices with 5 μg of exosomes from brain-tropic 231-BR (231 BrT1), lung-tropic 4175 (231 LuT1), bone-tropic 1833 (231 BoT1), or parental MDA-MB-231 (231 Parental) human breast cancer metastatic cells[6,15]

(Supplementary Fig. 1a), for two consecutive days, then added fluorescently-labelled 231 BrT1 cancer cells, measuring tumour cell colonization three days later (Supplementary Fig. 1b – cancer cell number). Pre-treatment of brain slices with 231 BrT1-derived exosomes increased colonizing 231 BrT1 cell number four-fold compared to PBS, and two-fold or more compared to pre-treatment with 231 parental and lung- or bone-metastatic exosomes (Fig. 1a), respectively. Pre-treatment with non-brain tropic exosomes did not induce significant cancer cell growth compared to PBS (Fig. 1a and Supplementary Fig. 1c).

Next, we asked if pre-conditioning with brain metastatic tumour-derived exosomes impacted brain metastatic cell invasiveness. Three days after tumour cell addition, we quantified invading 231 BrT1 cells in transversal sections of brain slices pre-treated with 231 BrT1 or 231 parental-derived exosomes (Supplementary Fig. 1b – cancer cell invasion) and determined that 231 BrT1 exosome pre-treatment augmented 231 BrT1 cell invasiveness three-fold compared to 231 parental-derived exosomes or PBS, respectively (Fig. 1b). Moreover, Ki-67 immunostaining showed that 231 BrT1 exosome pre-treatment bolstered invading 231 BrT1 cell proliferation over four-fold compared to 231 parental exosomes (Supplementary Fig. 1d). Remarkably, brain slice pre-conditioning with 231 BrT1-derived exosomes also enhanced colonization by 231 parental cells (Supplementary Fig. 1e), which have limited ability to generate brain metastases[4,7]. Brain slice pre-treatment with 231 BrT1-derived exosomes induced a five-fold and over two-fold increase in colonizing 231 parental cell number compared to PBS or 231 parental exosome pre-treatment, respectively (Supplementary Fig. 1e). Overall, pre-conditioning brain slices with brain metastatic cell-derived exosomes supported tumour colonization independent of cell-intrinsic brain metastatic potential, suggesting that exosome-mediated brain microenvironment remodeling supports metastatic cell proliferation and invasion.

Proteomic analysis identifies exosomal CEMIP as a brain metastatic protein

We previously showed tumour exosomes package specific proteins critical for the metastatic process at target organs[10,11] and that integrins are abundantly packaged in tumour exosomes that promote lung and liver metastasis[12]. Surprisingly, brain metastatic exosomes packaged few integrins and at low levels[12], albeit ones whose cellular expression had previously been associated with BrM: α2, α3, β3 and β1 integrins [16,17]. Thus, exosomal molecules other than integrins may support BrM. Quantitative mass spectrometry comparison of exosome proteomes from brain-tropic 231 BrT1 and BrT2 [831] to those of 231 parental, lung-tropic (LuT1 [4175]; LuT2 [4173]) and bone-tropic (BoT1 [1833]) MDA-MB-231 cells revealed that only twenty proteins were differentially expressed in brain tropic exosomes when compared to exosomes from parental cells (Fig. 1c; Supplementary Table 2). Among these, CEMIP or KIAA1199[18], emerged as a prominent exosomal protein in both brain metastatic models, with low or undetectable expression in exosomes from lung and bone metastatic models, suggesting a specific association with BrM potential. CEMIP is involved in hyaluronic acid depolymerization[19], intracellular calcium regulation[20] and Wnt signaling[21], playing multiple roles in cancer progression[22], inflammation[23], and interestingly, in normal brain physiology[24]. Western blot quantification of exosomal CEMIP confirmed high abundance in brain metastatic cell-derived exosomes compared to parental and non-brain metastatic cell-derived exosomes (Fig. 1d). Interestingly, CEMIP was enriched ten-fold in

231 BrT1 exosomes relative to 231 BrT1 cells, suggesting selective packaging in exosomes (Fig. 1d).

To investigate CEMIP association with extracellular vesicle (EV) fractions containing exosomes, we applied the 231 BrT1 EV pellet obtained from ultracentrifugation onto an iodixanol/Optiprep density gradient and quantified CEMIP expression in fractions positive for exosomal and small EV markers Syntenin-1, CD81, and HSP70 (fractions 6–9). CEMIP was detected in fractions 5–9 (Supplementary Fig. 1f), with the highest CEMIP expression in the exosome-containing fraction 7, corresponding to a density of 1.10 g/mL. This indicates that CEMIP expression is specifically associated with small EVs, that include exosomes and their subpopulations (exosome large, exosome small vesicles and exomere particles)[25], as opposed to non-EV protein aggregates or microvesicles. CEMIP was abundant in exosomes from additional orthotopic brain metastatic models: MDA-MB-231-HM breast and N2LA-BR lung cancer (Fig. 1e), further supporting the association of exosomal CEMIP with BrM potential. Taken together, our data identify CEMIP as a protein enriched in exosomes from brain metastatic cancer cells.

Exosomal CEMIP modulates the brain vascular niche to support metastasis

To determine whether CEMIP is required for exosome-mediated brain colonization, we targeted *CEMIP* in brain metastatic 231 BrT1 cancer cells using CRISPR/Cas9. Western blot confirmed a significant reduction in CEMIP expression in two 231 BrT1 single cell clones with complex *CEMIP* indels, KO1 and KO2, and their exosomes, compared to control BrT1 cells (WT) and exosomes (Supplementary Fig. 2a). Transmission electron microscopy (Supplementary Fig. 2b) and nanoparticle tracking analysis (Supplementary Fig. 2c) revealed that CEMIP targeting did not affect exosome morphology or size. In addition, protein levels (BCA protein assay; Supplementary Fig. 2c) and expression of CD81 or Syntenin-1 (Supplementary Fig. 2a) remained unaltered in 231 BrT1 CEMIP KO-derived exosomes, suggesting CEMIP loss does not alter exosomal protein packaging.

We next investigated the functional role of CEMIP in BrM. Although the overall cancer cell number on the surface of *ex vivo* brain slices was not significantly impacted by CEMIP loss (Supplementary Fig. 2d), 231 BrT1 CEMIP KO and WT cell morphology was distinct. Consistent with previous reports[4,7,16], brain metastatic 231 BrT1 cells presented a spindle-like morphology and when invading, consistently associated with and spread along brain endothelial cells (BrECs) (Supplementary Fig. 2e – right and left panels, full white arrows), a process known as vascular co-option[26]. Interestingly, 231 BrT1 CEMIP KO cells were rounder, lost spindle-like morphology (Fig. 2a, full white arrows) and displayed significantly impaired ability to associate with brain vasculature, with a 50% reduction in both co-opting and invading cancer cells compared to 231 BrT1 CEMIP WT cells (Fig. 2a, b). Despite diminished brain colonizing ability *ex vivo*, CEMIP ablation did not affect *in vitro* proliferation or invasion (Supplementary Fig. 2f, g) suggesting that CEMIP's role in BrM is dependent on the brain microenvironment. Collectively, these results indicate that CEMIP loss reduces the ability of brain metastatic cells to interact with brain vasculature and successfully invade the brain.

To evaluate the relative contributions of exosomal and cellular CEMIP to BrM, we investigated whether exosomal CEMIP was sufficient to rescue brain colonization, invasion and vascular co-option by 231 BrT1 CEMIP KO cells. Brain slice pre-treatment with 231 BrT1 CEMIP WT-derived exosomes induced a four-fold and two-fold increase in colonizing 231 BrT1 CEMIP KO2 cell number compared to PBS and CEMIP KO exosome pre-treatment, respectively (Supplementary Fig. 2h). More importantly, brain slice pre-treatment with 231 BrT1 CEMIP WT-derived exosomes restored 231 BrT1 CEMIP KO2 vascular co-option, and their characteristic spindle-like phenotype (Fig. 2c, full white arrows). Whereas 231 BrT1 CEMIP WT-derived exosomes increased cancer cell vascular co-option over two-fold, pre-treatment with CEMIP KO1 or KO2 exosomes did not (Fig. 2c). Moreover, pre-treatment with 231 BrT1 CEMIP WT-derived exosomes increased 231 BrT1 CEMIP KO2 invasion by three-fold compared to PBS and CEMIP KO exosome pre-treatment (Fig. 2d). These results suggest that exosomal CEMIP supersedes cellular CEMIP in promoting adaptation to the brain microenvironment via vascular co-option, ultimately supporting successful invasion and metastatic colonization of the brain.

Exosomal CEMIP supports brain colonization *in vivo*

Whereas the above illustrated that CEMIP promotes vascular co-option, invasion, and colonization, the data were confined to brain slices and thus bypassed critical steps of the metastatic cascade. Therefore, we used experimental metastasis assays to investigate whether CEMIP mediates BrM *in vivo*. Loss of cellular CEMIP led to a significant reduction in BrM four weeks following intracardiac injection of 231 BrT1 cells (Fig. 3a). Histology revealed a 70% decrease in brain metastatic foci generated by 231 BrT1 CEMIP KO *versus* CEMIP WT cells (Fig. 3a – bottom left graph) and a metastatic burden reduction in both CEMIP KO models relative to CEMIP WT, especially in KO1 (Fig. 3a – bottom right graph). However, we observed no significant differences in individual lesion size between CEMIP WT and CEMIP KO cells, suggesting that CEMIP is required during early steps of metastatic colonization. Accordingly, we found no significant difference in tumor outgrowth after intracranial injection upon CEMIP loss (Supplementary Fig. 3a), or in primary tumor growth after mammary fat pad injection (Supplementary Fig. 3b).

To determine if exosomal CEMIP affects BrM *in vivo*, we evaluated if pre-treatment of mice with 10μg of 231 BrT1 CEMIP WT or CEMIP KO-derived exosomes every other day for three weeks prior to intracardiac injection of 231 BrT1 GFP-luciferase^{+} cells enhanced BrM in a CEMIP-dependent manner. Pre-treatment with 231 BrT1 CEMIP WT-derived exosomes significantly boosted BrM compared to CEMIP KO1 and KO2 exosome pre-treatments at week one and two post-injection, ultimately normalizing over time since emerging CEMIP^{+} WT cells produce CEMIP^{+} exosomes (Fig. 3b – left graphs). Quantification of brain lesions revealed an increase in metastatic foci number and metastatic burden in CEMIP WT exosome pre-treated mice compared to PBS and one of the CEMIP KO exosome pre-treated groups (Fig. 3b –right graphs). Collectively, these data support a pro-metastatic role of exosomal CEMIP *in vivo* during the early stages of colonization and demonstrate that exosomal CEMIP promotes BrM *in vivo*.

Exosomal CEMIP induces remodeling and inflammation in the brain vascular niche

Since our findings suggest a critical role for exosomal CEMIP in the brain vascular niche, we sought to identify resident cells within the brain involved in this process. We treated brain slices with 5 μg of fluorescently-labelled 231 BrT1-derived exosomes and examined exosome uptake by endothelial cells, microglia, astrocytes and neurons, *via* immunofluorescence, 24 hours post-treatment (Fig. 4a and Supplementary Fig. 4a). Exosomes co-localized primarily with $CD31^+$ and $Glut1^+$ endothelial cells but were also uptaken by $Iba1^+$ microglia, including perivascular ones, and, to much lower extent, by $GFAP^+$ astrocytes and $NeuN^+$ neurons (Fig. 4a, b). These data are consistent with our previous work demonstrating that BrEC predominantly uptake tumour cell-derived exosomes *in vivo*[12] (Supplementary Fig. 4b). In addition, a single intracardiac injection of 10 μg of fluorescently-labelled 231 BrT1-derived exosomes disrupted blood-brain barrier vascular integrity, as evidenced by extravasated high molecular weight dextran in exosome-positive blood vessels (Supplementary Fig. 4c).

To determine whether exosomal CEMIP pre-conditioning led to vascular remodeling, we pre-treated murine BrEC *in vitro* with 10 μg of exosomes from CEMIP loss or gain of function models and evaluated vascular network formation in a 3D endothelial tube formation (ETF) assay 24 hours later (Supplementary Fig. 4d). To test if high exosomal CEMIP levels were sufficient to support vascular network formation, we overexpressed CEMIP in 231 parental cells (231 parental CEMIP OE) and their exosomes (Supplementary Fig. 4e). Pre-treatment with 231 parental CEMIP OE and 231 BrT1 CEMIP WT-derived exosomes promoted ETF, increasing the number and size of endothelial cell branches formed compared to 231 parental control and 231 BrT1 CEMIP KO exosomes (Fig. 4c). Consistent with these metrics, pre-treatment with exosomal CEMIP also increased segment junction number and decreased isolated segment number (Supplementary Fig. 4f). *In vivo*, in contrast to the surrounding normal brain tissue (empty white arrow), 231 BrT1 brain metastases had altered, morphologically heterogeneous vasculature with enlarged and dilated vessels (Supplementary Fig. 4g – full white arrows and graph), characteristic of metastatic lesions in the brain[27], while 231 BrT1 CEMIP KO metastatic lesions displayed significantly smaller vessel diameter, similar to the surrounding non-metastatic brain tissue. Collectively, these findings support a functional role for tumour cell-derived exosomal CEMIP in the remodeling of brain vasculature.

To dissect the molecular changes elicited by exosomal CEMIP during brain vascular niche remodeling, we analyzed the gene expression profiles of brain cells uptaking tumour exosomes, endothelial cells and microglia, the latter often observed in close contact with the brain vasculature (Fig. 4b, double white arrow) and known to play critical roles during vascular remodeling and dysfunction[28]. We isolated exosome-positive BrEC ($CD45^-$ $CD31^+$) and microglia ($CD45^+$ $CD11b^{low}$ $CD49d^{low}$) from brain slices pre-conditioned with 5 μg of fluorescently-labelled exosomes from either 231 BrT1 CEMIP WT or 231 BrT1 CEMIP KO cells and analyzed gene expression changes by RNA sequencing (Supplementary Fig. 4h). We observed no difference between the uptake of fluorescently-labelled 231 BrT1 CEMIP WT or 231 BrT1 CEMIP KO exosomes (Supplementary Fig. 4i), indicating that gene expression differences are not due to differential binding or uptake of

exosomes. Correspondingly, we observed no difference between 231 BrT1 CEMIP WT and CEMIP KO exosome adhesion to $CD31^+$ endothelial cells by immunofluorescence analysis (Supplementary Fig. 4j).

Analysis of gene expression changes induced by brain metastatic-derived exosomes in both endothelial cells and microglia (Supplementary Table 3 and 4) revealed activation of several signaling pathways related to inflammation and cancer metastasis (Supplementary Table 5). To identify genes modulated by exosomal CEMIP, we first focused on genes significantly altered by pre-treatment with 231 BrT1 CEMIP WT-derived exosomes compared to the PBS control and then on the genes that showed significant and concordant difference in expression when compared to pre-treatment with both 231 BrT1 CEMIP KO exosomes. Pre-treatment with 231 BrT1-derived exosomes changed the expression levels of 286 endothelial cell genes and 193 microglial genes (Supplementary Table 4), with a higher proportion of CEMIP-dependent changes in BrEC *versus* microglia (119 versus 25 genes, respectively; Supplementary Table 6). Gene ontology analysis of genes with altered expression upon $CEMIP^+$ exosome treatment identified blood vessel morphogenesis and lymphangiogenesis as the second and third most significantly affected processes in BrECs (Supplementary Table 7), while inflammatory responses were the top most significantly affected biological process in exosome-positive microglia (Supplementary Table 7). Ingenuity Pathway Analysis (IPA) identified 14 pathways significantly affected by exosomal CEMIP in BrEC, half of which were inositol-related pathways, which CEMIP impacts through intracellular calcium release[20,29] (Supplementary Table 5). CEMIP-dependent calcium signaling governs numerous cellular processes relevant for vascular remodeling and angiogenesis, such as cell migration and Wnt signaling[21,30], suggesting these gene expression changes may underlie the exosome-dependent vascular phenotypes we observed. Other CEMIP-dependent pathways were osteoarthritis (*Tcf7l1, Acvrl1, P2rx7, Prkab2* and *Sp1*), an inflammatory condition modulated by CEMIP as well as gap junction signaling (*Gja1, Npr2. Adcy4* and *Sp1*), and several adhesion molecules (e.g. *Efnb2, Nedd9, Itgb3, Acvrl1, Farp1, Synm, Sema6d, Ocln,* etc.), with roles in vascular remodeling and endothelial cell-cell contacts (Fig. 4d and Supplementary Table 4).

In microglia, IPA identified 69 exosomal CEMIP-dependent pathways, related to inflammation, immune regulation through cell adhesion and diapedesis (*Ccl5, Cxcl10, Cxcl1, Tnf and Tnfrsf1b*) and neuroinflammation (*Ccl5, Cxcl10, Ptgs2, Syk and Tnf*) (Fig. 4d and Supplementary Table 5). Taken together, these data demonstrate that exosomal CEMIP affects molecular pathways in BrEC and microglia implicated in BrM that may underlie reshaping of brain vascular niches and brain pre-metastatic niche formation.

CEMIP predicts brain metastasis and survival in patients

Next, we investigated the correlation between CEMIP protein levels in tissues and exosomes collected from cancer patients with brain metastases. We first characterized CEMIP expression by immunohistochemistry in tissue microarrays from over 300 samples of primary tumours (PTs) and metastatic tumours (MTs) from breast and lung cancer patients with metastases in the brain, metastases in other organs (e.g. bone, colon, heart, kidney, liver, lung, pleura, skin or stomach) or no metastases. Analysis of brain MTs revealed that tumour

CEMIP expression was markedly increased compared to surrounding brain stroma (Fig. 5a). Based on staining intensity, brain MTs were categorized into low (staining score 0–2) or high (staining score >2–4) CEMIP expression (Fig. 5b). Interestingly, analysis of CEMIP expression in PTs revealed that patients with BrM had significantly higher CEMIP expression ($CEMIP^{high}$ sample percentage: 32.4 for PTs Brain MET versus 12.0 and 13.5 for PTs Non-Brain MET and No MET, respectively; Fig. 5c; Supplementary Table 8) than PTs from patients with metastasis to organ sites other than the brain, or without metastasis, indicating PT CEMIP expression levels correlated with BrM but not with non-brain metastasis (Supplementary Table 9). Moreover, analysis of brain MTs showed significantly higher CEMIP expression compared to MTs from other organs (Fig. 5c). Consistently, more than 40% of brain MTs analyzed were $CEMIP^{high}$, whereas of all non-brain MTs only 7% were $CEMIP^{high}$ (Fig. 5c). Furthermore, for patients that developed brain metastases, high PT CEMIP expression correlated with a shorter latency period for metastasis (Fig. 5d). Moreover, patients with $CEMIP^{high}$ brain MTs had significantly poorer survival compared to patients with $CEMIP^{low}$ brain MTs (Supplementary Fig. 5a).

Similar to PTs and MTs of patients with brain metastases, CEMIP expression by immunohistochemistry was higher in cultured brain MT cells (Supplementary Fig. 5b), whose exosomes expressed high CEMIP by western blot (Fig. 1d). Evaluation of CEMIP expression in exosomes collected from 24-hour cultures of viable human brain MTs, as well as bone MTs, another common site of metastasis, revealed CEMIP in all human brain MT exosomes examined; but only in one of three bone MT-derived exosomes from lung cancer patients (Supplementary Fig. 5c). Western blot analysis of exosomal CEMIP from surgically resected early stage human NSCLC PTs revealed variable expression across patients, indicating exosomal CEMIP can be detected in PT-derived samples even at early stages and could therefore inform brain metastatic risk (Supplementary Fig. 5d). Collectively, our patient data demonstrated that CEMIP is expressed by brain MTs and their exosomes and that high CEMIP expression in PTs is associated with shorter latency to brain metastasis and poor patient survival.

DISCUSSION

Gaining insight into the mechanisms of BrM and the specific contribution of tumour-derived exosomes to this process provides opportunities for early diagnosis and therapeutic targeting of BrM. We now show that pre-conditioning the brain microenvironment with exosomes derived from brain metastatic cells generates a metastatic niche that supports colonization. We identified CEMIP, a protein expressed in the brain and involved in memory and synaptic formation[18,24], as specifically enriched in brain metastatic exosomes. While cellular expression of CEMIP has been previously associated with cancer progression[22] and inflammatory diseases[23,31], our study reveals a role for exosomal CEMIP in brain metastasis.

We demonstrate that CEMIP targeting impairs brain metastatic ability but not primary tumor growth, underscoring that CEMIP functions are exerted upon the brain microenvironment. CEMIP loss reduced the number of brain metastatic colonies formed in an experimental brain metastatic setting, but not *in situ* brain outgrowth, suggesting CEMIP is critical in the

early phases of brain colonization. Remarkably, exosomal CEMIP pre-conditioning enhanced brain metastatic colonization, restoring the ability of CEMIP-depleted cells to associate with brain vasculature.

Brain metastatic cancer cells often display angiocentric growth in the brain[26], hijacking existing vasculature and generating tortuous and enlarged vessels[27], typically through an angiogenic strategy known as non-sprouting or intussusceptive angiogenesis (IA). This is distinct from tumour neo-angiogenesis observed outside of the brain. Thus, IA allows incorporation and growth of host vasculature into developing metastases likely through the combined action of diverse tumour cell-surface receptors and tumour-secreted factors, however, its regulation remains mostly unexplored[32]. Our work showing exosomal CEMIP promotes vascular network formation and triggers a pro-inflammatory gene signature in the brain provides mechanistic insight into IA-dependent BrM. Vessel morphogenesis was among the top biological processes reprogrammed by exosomal CEMIP in BrECs and may underlie the changes in BrEC branching and metastatic vascular remodeling we observed. Exosomal CEMIP-dependent BrEC gene expression changes associated with inositol signaling, cell junction and adhesion (Fig. 4d) are consistent with previous studies demonstrating CEMIP interacts with inositol pathway-related proteins, promoting migration *via* calcium-mediated cytoskeletal re-arrangements, and stimulating vessel growth and enlargement *in vivo*. Exosomal CEMIP also led to Notch signaling inhibition and ephrin B2 downregulation in BrECs, both processes that stimulate IA[33], while in microglia it induced a pro-inflammatory signature consistent with neuro-inflammation mediated-IA[34].

Microglia, known players in brain microenvironment reshaping and BrM, exhibited gene expression alterations in additional inflammatory pathways involved in rheumatoid arthritis, neuroinflammation, immune cell adhesion and vascular transmigration. Exosomal CEMIP upregulated pro-inflammatory cytokines *Tnf*, *Ptgs2*, and *Ccl/Cxcl* in microglia, that promote BrM and blood-brain barrier dysfunction[35], consistent with the vascular leakiness induced by brain metastatic exosomes we and others have observed[36]. Our results also agree with recent findings that extracellular vesicles interact with blood vessel-associated microglia associated within primary brain tumours[37].

Taken together, our findings suggest that exosomal CEMIP induces a pro-inflammatory state in the brain vascular niche that supports brain metastatic colonization. A more detailed characterization of the pathways downstream of exosomal CEMIP should shed light on the contribution of Wnt signaling and intracellular calcium release for pre-metastatic niche formation in the brain.

The clinical relevance of CEMIP in BrM is underscored by significantly increased expression in human brain metastases, compared to adjacent brain stroma and non-brain metastatic lesions, and association with poor patient survival. Moreover, CEMIP expression at the PT level correlated with metastasis to brain but not other organs. Further, high levels of CEMIP expression were associated with rapid metastatic progression to the brain, suggesting that CEMIP may be a reliable biomarker of brain metastatic risk.

Overall, our findings identify role for CEMIP in BrM, suggesting it is a promising prognostic biomarker and therapeutic target for BrM. Our future studies will focus on circulating tumour-derived exosomal CEMIP as a plasma-based biomarker for non-invasively screening patients for primary and recurrent brain metastases, along with testing targeted therapies aimed at blocking CEMIP to halt BrM.

METHODS

Cell lines.

The breast cancer cell line MDA-MB-231 (parental) was purchased from ATCC. The following MDA-MB-231 organotropic derivative cell lines were provided: 231BR (brain-tropic, BrT1) by P. Steeg (NCI); 831 (brain-tropic, BrT2), 4175 (lung-tropic, LuT1) and 1833 (bone-tropic, BoT1) by J. Massagué (MSKCC); 4173 (lung-tropic, LuT2) by A. Minn (University of Pennsylvania); and MDA-MB-231-HM (brain-tropic) by S. Wang (UC San Diego) (Supplementary Fig. 1a and references therein). The brain metastatic derivative N2LA-BR of the lung cancer cell line N2LA was generated from a metastatic lung cancer patient by V. Rajasekhar (MSKCC). Breast and lung cancer cells were cultured in DMEM or RPMI, respectively, with 10% fetal bovine serum (FBS), and Penicillin/Streptomycin. For exosome isolation from culture supernatants, cells were cultured in exosome-depleted FBS[10–12]. Cells were maintained in a humidified 37°C incubator with 5% CO_2. Cell lines routinely tested negative for mycoplasma.

Exosome purification, labelling, and characterization.

Exosomes from cell lines were purified by ultracentrifugation[10–12]. Cell culture supernatant was centrifuged at 500*x*g, 10 min and then at 12,000*x*g, 20 min. Exosomes were collected by ultracentrifugation of this supernatant at 100,000*x*g, 70 min and the pellet washed by resuspending in PBS and re-ultracentrifuging at 100,000*x*g, 70 min. For imaging, exosomes were fluorescently-labelled using PKH67 or PKH26 lipophilic membrane dyes (Sigma) or CellVue Maroon (Polysciences) and PBS-washed[10–12]. Unlabelled or labelled exosomes were resuspended in PBS for experiments.

Exosome protein concentration was determined by BCA assay (Pierce, Thermo Scientific). Exosome size and particle number were analyzed using the DS500 nanoparticle characterization system (NanoSight, Malvern Instruments)[12]. Exosomes were imaged by negative stain transmission electron microscopy[25].

Brain slice assay.

Organotypic brain slice cultures were adapted from a previously described protocol for generation of mouse brain cortical slices to study neuron development[14]. Brains from 6–8 week-old athymic NCr nude (Taconic) or outbred *Foxn*$^{-/-}$ (Jackson Laboratories, #007850) female mice were dissected in complete HBSS (HBSS supplemented with HEPES (pH 7.4, 2.5mM); D-glucose (30mM); $CaCl_2$ (1mM); $MgSO_4$ (1mM); and $NaHCO_3$ (4mM)), after whole-body PBS perfusion. Fresh brains were embedded in microwave-preheated 4% low-melting agarose (Lonza) in complete HBSS once the agarose cooled to 37°C. Once solidified, embedded brains were cut into 250 μm coronal slices (bregma −2mm to +2mm)

using a VT 12000s vibratome (Leica). Slices were dissected across the midline separating brain hemispheres, generating symmetric halves. Brain slices damaged during sectioning/handling were discarded. Slices generated from different positions across the brain anterior-posterior axis were distributed equally to ensure experimental groups contained an identical collection of slices representative of the brain region sectioned. Groups of three half-brain slices were placed flat on top of 0.4 μm pore polycarbonate (PC) membrane cell culture inserts (#Z353086 Sigma or #140660 Thermo Scientific) in 6-well plates with media (DMEM with 25% complete HBSS, 5% FBS, L-glutamine (1mM), Penicillin/Streptomycin, and Normocin (Invivogen, 50 μg/mL)) in the bottom well. To establish and ensure a well-defined region for exosome and cancer cell administration to brain slices, a sterilized transparent PC ring (Small Parts) with a 3 mm inner diameter was placed on top of each slice. Rings were centrally positioned so that the inner-limit of the ring was within the slice boundaries.

For exosome and cancer cell administration, 3 μL of PBS-resuspended exosomes (5 μg), 7,500 BrT1 cells, or 20,000 parental cells were added inside the rings. For colonization studies, slices were pre-treated with PBS or exosomes for two consecutive days prior to adding cells to ensure that exosome-induced changes resulted from effects on the brain microenvironment. Cancer cells were added 24 hours after exosome treatment and incubated for 72 hours. Brain slices were maintained in a humidified 37°C incubator with 5% CO_2 for up to 5 days, changing media every two days. At endpoint, slices were washed with PBS before fixation in 2% paraformaldehyde for 2 hours at 4°C. Tissue processing and immunofluorescence are described below.

Tumour cell colonization was quantified by averaging the number of cancer cells growing on top of slices. Cell invasion was quantified by averaging the number of invading cancer cells observed below the first layer of brain cells on transversal sections of slices. Tumour cell interaction with vessels in the brain microenvironment was measured by quantifying the average number of spindle-like cells growing on top of slices in association with vessels. Cancer cells were counted manually with the multi-point tool in ImageJ software (version 1.52a).

For exosome adhesion and uptake, co-localization of exosomes and resident brain cells was evaluated after one treatment with fluorescently-labelled exosomes (5 μg). Slices were incubated with exosomes for 12 hours for adhesion studies or 24 hours for uptake studies, and then washed, fixed, and processed for immunofluorescence.

Proteomics.

Mass spectrometry of exosomes was performed at the Rockefeller University Proteomics Resource Center, as described[12]. Data were quantified and searched against Human Uniprot database (July 2014) using MaxQuant (version 1.5.0.9). Perseus software (version 1.5.0.9) was used for bioinformatics and statistical analysis. Protein abundances were expressed as LFQ (label free quantitation) values. Only proteins quantified in at least two of three replicates in at least one group were retained, and missing values were imputed. An ANOVA test was performed and corrected for multiple hypotheses testing using a permutation-based FDR threshold of 0.05. GENE-E software was used for heatmap generation and data display.

Mass spectrometry data have been deposited in ProteomeXchange with the primary accession code PXD015210.

Immunoblotting.

Exosomes and cells lysed with RIPA buffer plus protease inhibitor cocktail were diluted with sample buffer, run on Novex 4–12% Tris-Glycine Gels (Life Technologies), and transferred onto PVDF membrane. Proteins were detected with primary antibodies and HRP-conjugated secondaries (Jackson Immunoresearch), and imaged by enhanced chemiluminescence. Antibodies can be found in Supplementary Table 10. For CEMIP quantification, the ratio between the CEMIP and ACTB band intensities for each sample was measured using ImageJ software.

Exosome OptiPrep™ density gradient.

To prepare the discontinuous iodixanol gradient, 40% (w/v), 20% (w/v), 10% (w/v) and 5% (w/v) iodixanol solutions were made by diluting OptiPrep™ (60% (w/v) aqueous iodixanol from Sigma) with 0.25 M sucrose/10 mM Tris, pH 7.5. Three milliliters of 40% iodixanol solution were added to a 14 × 95 mm ultra-clear tube (Beckman Coulter), followed by layering 3 mL each of 20% and 10% solutions and 2.5 mL of 5% solution. Exosomes in 500uL of PBS were overlaid onto the top of the gradient. A portion of the exosome sample was saved as input. The gradient was centrifuged at 100,000*x*g,16 hours at 10 °C using a SW-40 Ti Rotor. Twelve 1 mL gradient fractions were collected from top to bottom, diluted with PBS, centrifuged at 100,000xg, 3 hours at 10 °C, and resuspended in RIPA buffer. Density was determined by measuring the weight of each fraction (g/mL) (Supplementary Fig. 1f and references therein).

Mouse studies.

Mouse work was performed in accordance with institutional, IACUC and AAALAS guidelines (Weill Cornell Medicine animal protocol 0709–666A) and the study is compliant with all relevant ethical regulations regarding animal research. Animals were monitored for stress, illness or abnormal tissue growth, and euthanized if health deteriorated. Mice that died before the experimental endpoint were excluded from the analysis. Experiments used 6–8 week-old athymic NCr nude or outbred *Foxn*$^{-/-}$ mice. At endpoints, mice were euthanized, perfused with PBS, and tissues were collected. No statistical method was used to pre-determine sample size and no method of randomization was used to allocate animals to experimental groups.

For *in vivo* exosome distribution, brains were collected 24 hours post-intracardiac injection of fluorescently-labelled exosomes (10 ug). Uptake by brain cells was evaluated by immunofluorescence. To evaluate exosome-induced vascular leakiness, Texas-Red-lysine fixable dextran 70,000 MW (Invitrogen) (2 mg) was retro-orbitally injected 23 hours after treatment with PKH67-labelled exosomes (10 μg). One hour post-dextran injection, brain tissue was collected for analysis of extravasated dextran and exosome localization.

For experimental brain metastasis, 1×10^4 GFP-labelled and/or luciferase-expressing BrT1 cells in PBS were intracardiacally injected. For experimental brain metastasis *in situ* growth,

1×10^5 GFP/luciferase-expressing BrT1 cells in 2 μL of PBS were intracranially injected in the right brain hemisphere using a low-volume Hamilton syringe and stereotactic apparatus. Cells were injected at a rate of 0.2 μL/min, at 2.5 mm depth from the surface of the brain and coordinates 0.1 mm posterior and 2.0 mm lateral to the bregma. For orthotopic primary tumour growth, 1×10^6 BrT1 cells in Matrigel (Corning) were injected into the 4th mammary fat pad.

For experimental brain metastasis exosome education, exosomes (10 μg) were retro-orbitally injected every other day for three weeks, mimicking continuous and systemic exosome release by primary tumours[10,12]. One day after the last treatment, mice were intracardiacally injected with 1×10^4 BrT1 GFP/luciferase-expressing cells in PBS.

IVIS SpectrumCT bioluminescence imaging system (PerkinElmer) was used for *in vivo* brain metastasis imaging. *In vivo* cranial bioluminescence was analyzed by total cranial photon flux (p/s) quantification using Living Image software (Caliper Life Sciences). Negative p/s values were considered zero. Brain metastases in sagittal brain sections were analyzed by histological evaluation and quantification of lesion number and total brain metastatic lesion area, scoring two whole brain sagittal sections from different brain areas per mouse, stained with anti-GFP and DAPI or H&E. Tumour cell clusters with 10 or more cells were considered as metastatic foci. Orthotopic primary tumour size was measured manually with a vernier caliper. Tumour volume was calculated using the formula for an ellipsoid, $V = \pi/6\ (L \times W \times H)$ (Supplementary Fig. 3b and references therein).

Tumour vasculature caliber was determined by measuring vessel diameter within metastatic foci and neighboring normal brain regions, in two whole brain sagittal sections from different brain areas per individual using ImageJ software. Vessel diameter was calculated as the average of three measurements along the vessel, scoring up to five different tumour/normal vessels per individual, evaluating metastatic foci within the same size range across groups.

Tissue processing and immunostaining.

For histological analysis of exosome and brain metastasis, freshly dissected brains were embedded and frozen in in Tissue-tek OCT (Electron Microscopy Sciences). Lungs and other organs were fixed in 4% paraformaldehyde overnight at 4°C before freezing in OCT.

For immunofluorescence, cryosections were permeabilized in PBS with 0.25% Triton X-100 (PBS-T), blocked in PBS-T with 3% bovine serum albumin and 5% normal goat serum and incubated overnight at 4°C in blocking solution with primary antibodies (Supplementary Table 10). Samples were incubated with secondary antibodies conjugated to AMCA, Alexa Fluor 488, 568 or 647, DAPI-stained, and mounted with Prolong Diamond antifade (Invitrogen). For histological analysis of brain metastasis with H&E, brains were fixed in 4% paraformaldehyde overnight at 4°C and processed for paraffin embedding. Sections were stained and mounted with VectaMount medium (Vector).

For brain slices, the PC ring was removed and slices were PBS washed. Immunofluorescence was carried out in free-floating conditions using the same protocol for

tissue sections. For invasion, fixed slices were washed in PBS, outer-ring regions were dissected out and tissue was embedded in OCT and frozen. Cryosections perpendicular to the plane of the slice were immunostained as for tissue sections.

CEMIP knockout and overexpression.

CEMIP knockout in BrT1 cells was achieved by transfection of cells using Lipofectamine LTX/PLUS (Invitrogen, 15338100) with PX458-DsRed-Cas9 vector carrying gRNAs (Supplementary Table 10) targeting human CEMIP. Vectors were prepared by MSKCC Gene Editing and Screening Core Facility, and sgRNAs were chosen using Guidescan (MSKCC). DsRed-expressing cells were single cell-sorted into 96-well plates for clonal growth. CEMIP depletion was evaluated by immunoblot and validation of CEMIP gene editing was verified by Sanger sequence identification of complex indels.

CEMIP was overexpressed in 231 parental cells by lentiviral transduction. Full length human CEMIP was PCR-amplified (Supplementary Table 10) from pcDNA3.2V5DEST_wtKIAA1199 (a gift from Dr. G. Marra, Institute of Molecular Cancer Research, University of Zurich) and subcloned into SalI/XbaI sites of pLentiCMV-blast (provided by E. Campeau, University of Massachusetts Medical School; Addgene #17486) (Supplementary Fig. 4e and references therein). As a control, parental cells were infected with pLentiCMV-blast empty-vector lentivirus. Lentivirus was produced using a third-generation system by co-transfecting HEK-293T cells using Lipofectamine LTX/PLUS with expression cDNA and packaging/envelope plasmids (pRSV-REV, pMD2Lg/pRRE, and pMD2.g, provided by D. Trono, École Polytechnique Fédérale de Lausanne; Addgene #12253, #12251, and #12259). Cells were infected overnight with virus. Stable cell lines were selected with blasticidin, and overexpression was confirmed by immunoblot.

Proliferation and invasion assays.

For proliferation, 2×10^6 BrT1 cells were plated in T175 flasks and counted 72 hours post-seeding. For invasion, cells were serum-starved for 24 hours pre-plating, and 2.5×10^4 cells were seeded in Matrigel-coated transwell inserts (8-μm pore size, Corning). Cell suspensions were added to inserts containing media with 1% FBS on the top and media with 10% FBS in the bottom chamber and were incubated at 37°C for 48 hours. Cells that remained in the upper chamber were removed with cotton swabs. Inserts were fixed with 1% paraformaldehyde overnight at 4°C and mounted with Prolong Gold antifade reagent with DAPI (Invitrogen) for visualization.

Brain endothelial cells.

Brain endothelial cells (BrECs) were isolated from young adult C57BL/6J mouse brains with a collagenase/dispase solution and cultured (Supplementary Fig. 4d and references therein). Cells were plated on fibronectin-coated plates (Sigma, 1 mg/mL in PBS) in mEC media. BrECs were selected with puromycin-containing media up to the first passage. BrECs were infected with E4ORF1-carrying lentivirus 96 hours post-isolation to enable robust expansion (Supplementary Fig. 4d and references therein). Accutase was used for cell detachment and endothelial purity was confirmed by expression of VE-Cadherin and CD31

and absence of CD45. BrECs were maintained in a humidified 37°C incubator under hypoxic conditions (5% O_2) and 5% CO_2.

For assays, cells were sub-cultured in Advanced DMEM/F12 with 20% exosome-depleted FBS, 1% Antibiotic-Antimycotic (Invitrogen), 1% Glutamax (Life Technologies), 1% Non-essential Amino Acids (Life Technologies), 1% CD Lipid Concentrate (Life Technologies), HEPES (20mM), Heparin (100 μg/mL), Endothelial cell mitogen (Alfa Aesar, 50 μg/mL), and SB431542 (R&D systems, 5 μM). BrECs were grown to 80% confluence and starved in 5% FBS for 6 hours pre-exosome treatment. The Cultrex In Vitro Angiogenesis Assay tube formation kit (Trevigen) was used for tube formation. 1×10^4 calcein AM-labelled BrECs, pre-treated for 24 hours with PBS or exosomes (10 μg), were seeded in μ-Slide Angiogenesis chambers (Ibidi) and allowed to form vascular networks for 4 to 6 hours. Images of vascular networks were analyzed with ImageJ's tool "Angiogenesis Analyzer" (by Gilles Carpentier) to quantitate the number of junction elements (corresponding to nodes or groups of fusing nodes – pixels with 3 neighbors), number and length of branches (elements of a ramification delimited by a junction and one extremity) or isolated segments (binary lines that are not branched or connected to other vascular structures) allowed overall assessment of topology and complexity of the vascular meshed network formed.

Image acquisition.

Pictures were taken as follows: with an E800 Eclipse microscope (Nikon) at 400x magnification to analyze *in vivo* exosome distribution, exosome-induced vascular leakiness, and *in vitro* CEMIP immunohistochemistry; with an EVOS FL Cell Imaging System microscope (Thermo Scientific) at 260x magnification to analyze *ex vivo* brain slice exosome uptake, cancer cell colonization and invasion, *in vitro* BrEC ETF, and *in vivo* brain metastatic vasculature; with a Panoramic Flash slide scanner (3DHistech) at 20x magnification to analyze brain metastatic colonization in whole brain slices and whole brain sagittal sections; with a TCS SP5-II confocal microscope (Leica Microsystems) to analyze *ex vivo* exosome adhesion and uptake.

FACS.

Brain slices were pre-treated with PBS or PKH67-labelled exosomes (5 μg/slice) for two consecutive days, the outer-ring areas were dissected out and the PC ring removed. Tissue was washed with PBS before Dispase/Collagenase (Roche; Dispase II at 1 U/mL and Collagenase A at 2.5mg/mL final concentration) digestion for 15 minutes at 37°C with agitation (70 RPM). Single-cell suspensions were obtained by pipetting and filtering through a 100μm cell strainer. Cells were washed with MACS buffer (PBS Ca^{2+}/Mg^{2+}-free, 1% Bovine Serum Albumin, 2mM EDTA), collected by centrifugation at 300*x*g, 5 min at 4°C, and incubated with Myelin Removal Beads (Miltenyi). Myelin-free cells were resuspended in MACS buffer and incubated with fluorescently-labelled antibodies (Supplementary Table 10) for 30 min at 4°C: CD45, CD31, CD11b, and CD49d. BrECs were defined as $CD45^-$ $CD31^+$ and microglial cells as $CD45^+$ $CD11b^{low}$ $CD49d^{low}$ (Supplementary Fig. 4h and references therein). Cells were washed with MACS buffer, filtered through a 40μm strainer and DAPI-stained. Unstained and single-stained cells/beads were used for cell sorter set-up. $DAPI^+$ dead cells were excluded. Sorting was performed on a FACS Aria (Becton

Dickinson) and exosome positive BrECs and microglia cells were sorted into RLT buffer (Qiagen) with 2-Mercaptoethanol and frozen. Becton Dickinson Diva Software was used for cell sorting and data acquisition and TreeStar FlowJo 10.5.3 was used for data analysis.

RNA sequencing.

RNA was extracted from cells using the RNeasy Micro kit (QIAGEN) and quantified using Qubit 2.0 Fluorometer (Life Technologies). RNA integrity was checked with TapeStation (Agilent Technologies). GENEWIZ, LLC. (South Plainfield, NJ, USA) prepared RNA libraries and performed sequencing on the Illumina HiSeq instrument using HiSeq Control Software. Samples were sequenced using a 2×150 Paired End (PE) configuration. Raw sequence data (.bcl files) generated from Illumina HiSeq was converted into fastq files and de-multiplexed using the Illumina bcl2fastq v. 2.17 program. One mismatch was allowed for index sequence identification. After demultiplexing, sequence data was checked for overall quality and yield. RNA expression analysis methods and code are described in detail at doi: 10.5281/zenodo.3334930, complete all scripts used. Briefly, fastq file quality was evaluated with FastQC, followed by read trimming using Trimmomatic. Reads were aligned to *Mus musculus* GRCm38.p6 using Salmon. DESeq2 assessed differential gene expression among conditions using the Likelihood Ratio Test (LRT) and controlling for replicates. Sample clustering using Principal Component Analysis and sample clustering of variance stabilized transformed read counts identified two outliers – WT replicate C and KO2 replicate A – which were removed from further analysis. A post-hoc binomial Wald test in DESeq2 evaluated differences between PBS, WT, KO1 and KO2. The focal gene set of interest was identified as those genes for which: a) the likelihood ratio test was significant ($p \leq 0.05$); b) there were significant expression differences between WT and PBS ($p \leq 0.05$); c) WT expression was significantly different from both KO1 and KO2 ($p \leq 0.05$ in each contrast); and d) expression was concordantly up- or down-regulated in KO1 and KO2 relative to WT. Log2(Fold change) values and p values are reported according to the Wald tests. Ingenuity Pathway Analysis (IPA, Qiagen, version 01–13) was used for pathway analysis of gene expression data. RNA-seq data that support the findings of this study have been deposited in the Gene Expression Omnibus (GEO) under accession code GSE136628.

Human studies.

Tissue microarray-based studies and fresh tissue studies were conducted in accordance with Weill Cornell Medicine IRB-approved protocols (IRB #0604008488, #1312014589, #0411007570, and #0607008642) with informed consent or with HIPAA waiver of consent. The study is compliant with all relevant ethical regulations regarding research involving human participants. For the archival tissue microarray studies, samples from 317 distinct tumour resections (213 primary tumours and 104 metastatic tumours) over 278 unique patients were used. At the time of their surgery, patients ranged in age from 28 to greater than 89 years. 100% of breast carcinoma samples and 45% of lung carcinoma samples were derived from female patients. All patients used for this study had been diagnosed with invasive breast carcinoma (35% of samples) or non-small cell carcinoma of the lung (65% of samples). Within the lung carcinoma cohort, 72% of patients were diagnosed with adenocarcinoma, 15% with squamous cell carcinoma, and the remainder with non-small cell carcinoma. Additional details regarding human samples analyzed can be found in the results

and methods section of the manuscript, the figure legends, and the supplementary source data file on patient samples.

Tissue microarrays from primary tumour (PT) and metastatic tumour (MT) were generated from paraffin-embedded archival samples approved for research use through the Institutional Review Board at Weill Cornell Medicine. Blocks were cored in representative areas and H&E stained to confirm presence of tumour. Immunohistochemistry was performed on a Leica Bond system using the standard protocol F. Heat-mediated antigen retrieval was performed with Sodium Citrate buffer, pH 6 for 30 min, then samples were incubated with anti-CEMIP/KIAA1199 for 25 min at RT and detected with DAB. Sections were then counterstained with hematoxylin and mounted with Leica Micromount. Tumour cores (1 – 3 per sample) were scored for CEMIP staining intensity in tumour by two pathologists (D.P. and N.N.) on a scale from zero (no expression) to four (very high expression). For samples with more than one core available, average intensity was calculated. Based on CEMIP expression observed across different tumour samples, pathologists defined a threshold cutoff expression value (CEMIPexp>2) and assigned a binary score ($CEMIP^{low/high}$) to samples. Cases in which brain metastasis coincided with or preceded primary diagnosis or for which there was no information regarding time of primary diagnosis, were excluded from survival analyses. Progression Free Survival was based on $CEMIP^{low/high}$ expression in PT and defined as the duration between PT diagnosis and the earliest brain metastasis detected. Cases with >10 years from PT diagnosis to brain metastasis were omitted from analysis. Overall Survival was based on $CEMIP^{low/high}$ expression in brain MT and defined as the duration between PT diagnosis and patient date of death or last follow-up. Kaplan-Meier survival curves were compared using Log-rank (Mantel-Cox) test. Correlation of PT CEMIP expression with metastatic status (overall metastasis, non-brain metastasis, and brain metastasis) was determined by calculating the Spearman correlation coefficient.

For analysis of exosomes from surgically-resected fresh tumour samples, tissue was received within two hours post-surgery, dissected into $2mm^2$ pieces and cultured in serum-free DMEM media with L-glutamine (1mM) and Penicillin/Streptomycin. Cultures were maintained in a humidified 37°C incubator with 5% CO_2 and exosomes were isolated from the culture supernatant after 24 hours. Exosomal CEMIP expression was analyzed by immunoblot.

Statistics and Reproducibility.

Error bars in graphs represent mean±SEM. The number of independent biological replicates for each experiment and the sample size of each experimental group/condition are provided in figure legends. Statistical significance was determined with two-tailed Student’s t-test or one-way ANOVA. $P<0.05$ was considered statistically significant. Variance was similar between compared groups. The experiments were repeated independently with similar results. Prism 8 (version 8.0.2) was used for statistical analysis and graphing (Graphpad software). ImageJ (version 1.52a) was used for image processing and analysis. Photoshop CC (version 20.0.3, Adobe) and Illustrator CC (version 23.0.2, Adobe) were used for image editing and presentation.

Data availability.

RNA-seq raw data that support the findings of this study have been deposited in the Gene Expression Omnibus (GEO) under accession code GSE136628. Mass spectrometry raw data have been deposited in ProteomeXchange with the primary accession code PXD015210. The mass spectrometry processed data of MDA-MB-231 parental [Parental], brain-tropic (231-BR [BrT1] and 831 [BrT2]), lung-tropic (4175 [LuT1] and 4173 [LuT2]) and bone-tropic (1833 [BoT1]) exosomes (Fig. 1c) is available in Supplementary Table 2. The RNA sequencing processed data from Fig. 4d and Supplementary Tables 4–7, for murine brain endothelial cells and microglia cells isolated from *ex vivo* brain slices treated with PBS, 231 BrT1 WT, 231 BrT1 CEMIP KO1 and KO2 exosomes is available as Supplementary Table 3. The patient processed data from Fig. 5 and Supplementary Fig. 5 is available as Supplementary Table 8. Unprocessed scans and replicates for all immunoblots presented in the manuscript are available as Supplementary Figure 6.

Supplementary Material

Refer to Web version on PubMed Central for supplementary material.

ACKNOWLEDGEMENTS

We thank M. Ginsberg, G. Marra, P. Raju and T. Milner for reagents and expert advice; L. Nogues Vera, M. Teixeira and S. Grass for help in the lab; M. Schaeffer for proofreading; T. Zhang and K. Gyan for help with bioinformatics analysis; L. Cohen-Gould, the MSKCC Molecular Cytology Core Facility and K. Uryu for imaging counseling; T. Miller and F. Fang at the MSKCC Flow cytometry Core Facility, and T. Baumgartner at the Weill Cornell Medicine Flow Cytometry Core, as well as R. Bowman, for expert cell sorting; and the MSKCC Gene Editing and Screening Core Facility for molecular cloning and gene editing advice. The authors gratefully acknowledge support from the following funding sources: the National Cancer Institute (CA169538 to D.L. and M.J.B and CA232093 to D.L.), the US Department of Defense (W81XWH-13–1-0427 to D.L.), the Breast Cancer Research Foundation (to D.L. and C.M.G.), the Champalimaud Foundation, and the Daedalus Fund for Innovation (Weill Cornell Medicine, to D.L), the Children's Cancer and Blood Foundation, the Pediatric Oncology Experimental Therapeutics Investigator's Consortium Foundation, the Nancy C. and Daniel P. Paduano Foundation, the Eileen and James A. Paduano Foundation, the Sohn Foundation, the Hartwell Foundation, the Manning Foundation, the Thompson Foundation, the Malcolm Hewitt Wiener Foundation and the Tortolani Foundation. G.R. has been supported by a Peter Oppenheimer Fellowship, awarded by the American Portuguese Biomedical Research Fund and by the Fundação para a Ciência e a Tecnologia from Portugal. A.H. was supported by a Susan Komen Foundation For the Cure Fellowship. H.P. is supported by grants from MINECO (SAF2014–54541-R), Fundación Fero, Asociación Española Contra el Cáncer and Worldwide Cancer Research. C.M.G is supported by a US Department of Defense Breast Cancer Research Program Era of Hope Scholar Award (W81XWH-15–1-0201), the US National Cancer Institute (CA193461–01), the National Breast Cancer Coalition's Artemis Project and the Pink Gene Foundation.

ABBREVIATIONS

BrM	brain metastasis
CEMIP	cell migration-inducing and hyaluronan-binding protein
EV	extracellular vesicle
BrECs	brain endothelial cells
ETF	endothelial tube formation
PT	primary tumour

MT	metastatic tumour
IA	intussusceptive angiogenesis
FOV	field of view
SEM	standard error of the mean
FBS	fetal bovine serum
PC	polycarbonate
FACS	fluorescence-activated cell sorting

REFERENCES

1. Valastyan S & Weinberg RA Tumor metastasis: molecular insights and evolving paradigms. Cell 147, 275–292, doi:10.1016/j.cell.2011.09.024 (2011). [PubMed: 22000009]
2. Maher EA, Mietz J, Arteaga CL, DePinho RA & Mohla S Brain metastasis: opportunities in basic and translational research. Cancer Res 69, 6015–6020, doi:10.1158/0008-5472.CAN-08-4347 (2009). [PubMed: 19638593]
3. Eichler AF et al. The biology of brain metastases-translation to new therapies. Nat Rev Clin Oncol 8, 344–356, doi:10.1038/nrclinonc.2011.58 (2011). [PubMed: 21487419]
4. Valiente M et al. Serpins promote cancer cell survival and vascular co-option in brain metastasis. Cell 156, 1002–1016, doi:10.1016/j.cell.2014.01.040 (2014). [PubMed: 24581498]
5. Sevenich L et al. Analysis of tumour- and stroma-supplied proteolytic networks reveals a brain-metastasis-promoting role for cathepsin S. Nat Cell Biol 16, 876–888, doi:10.1038/ncb3011 (2014). [PubMed: 25086747]
6. Bos PD et al. Genes that mediate breast cancer metastasis to the brain. Nature 459, 1005–1009, doi:10.1038/nature08021 (2009). [PubMed: 19421193]
7. Lorger M & Felding-Habermann B Capturing changes in the brain microenvironment during initial steps of breast cancer brain metastasis. Am J Pathol 176, 2958–2971, doi:10.2353/ajpath.2010.090838 (2010). [PubMed: 20382702]
8. Thery C, Ostrowski M & Segura E Membrane vesicles as conveyors of immune responses. Nat Rev Immunol 9, 581–593, doi:10.1038/nri2567 (2009). [PubMed: 19498381]
9. Peinado H et al. Pre-metastatic niches: organ-specific homes for metastases. Nat Rev Cancer, doi:10.1038/nrc.2017.6 (2017).
10. Peinado H et al. Melanoma exosomes educate bone marrow progenitor cells toward a pro-metastatic phenotype through MET. Nat Med 18, 883–891, doi:10.1038/nm.2753 (2012). [PubMed: 22635005]
11. Costa-Silva B et al. Pancreatic cancer exosomes initiate pre-metastatic niche formation in the liver. Nat Cell Biol 17, 816–826, doi:10.1038/ncb3169 (2015). [PubMed: 25985394]
12. Hoshino A et al. Tumour exosome integrins determine organotropic metastasis. Nature 527, 329–335, doi:10.1038/nature15756 (2015). [PubMed: 26524530]
13. Lowery FJ & Yu D Brain metastasis: Unique challenges and open opportunities. Biochim Biophys Acta Rev Cancer 1867, 49–57, doi:10.1016/j.bbcan.2016.12.001 (2017). [PubMed: 27939792]
14. Polleux F & Ghosh A The slice overlay assay: a versatile tool to study the influence of extracellular signals on neuronal development. Sci STKE 2002, pl9, doi:10.1126/stke.2002.136.pl9 (2002). [PubMed: 12060788]
15. Yoneda T, Williams PJ, Hiraga T, Niewolna M & Nishimura R A bone-seeking clone exhibits different biological properties from the MDA-MB-231 parental human breast cancer cells and a brain-seeking clone in vivo and in vitro. J Bone Miner Res 16, 1486–1495, doi:10.1359/jbmr.2001.16.8.1486 (2001). [PubMed: 11499871]

16. Carbonell WS, Ansorge O, Sibson N & Muschel R The vascular basement membrane as “soil” in brain metastasis. PLoS One 4, e5857, doi:10.1371/journal.pone.0005857 (2009). [PubMed: 19516901]
17. Lorger M, Krueger JS, O’Neal M, Staflin K & Felding-Habermann B Activation of tumor cell integrin alphavbeta3 controls angiogenesis and metastatic growth in the brain. Proc Natl Acad Sci U S A 106, 10666–10671, doi:10.1073/pnas.0903035106 (2009). [PubMed: 19541645]
18. Abe S, Usami S & Nakamura Y Mutations in the gene encoding KIAA1199 protein, an inner-ear protein expressed in Deiters’ cells and the fibrocytes, as the cause of nonsyndromic hearing loss. J Hum Genet 48, 564–570, doi:10.1007/s10038-003-0079-2 (2003). [PubMed: 14577002]
19. Yoshida H et al. KIAA1199, a deafness gene of unknown function, is a new hyaluronan binding protein involved in hyaluronan depolymerization. Proc Natl Acad Sci U S A 110, 5612–5617, doi:10.1073/pnas.1215432110 (2013). [PubMed: 23509262]
20. Evensen NA et al. Unraveling the role of KIAA1199, a novel endoplasmic reticulum protein, in cancer cell migration. J Natl Cancer Inst 105, 1402–1416, doi:10.1093/jnci/djt224 (2013). [PubMed: 23990668]
21. Birkenkamp-Demtroder K et al. Repression of KIAA1199 attenuates Wnt-signalling and decreases the proliferation of colon cancer cells. Br J Cancer 105, 552–561, doi:10.1038/bjc.2011.268 (2011). [PubMed: 21772334]
22. Zhang Y, Jia S & Jiang WG KIAA1199 and its biological role in human cancer and cancer cells (review). Oncol Rep 31, 1503–1508, doi:10.3892/or.2014.3038 (2014). [PubMed: 24573670]
23. Yang X et al. KIAA1199 as a potential diagnostic biomarker of rheumatoid arthritis related to angiogenesis. Arthritis Res Ther 17, 140, doi:10.1186/s13075-015-0637-y (2015). [PubMed: 26022278]
24. Yoshino Y et al. Distribution and function of hyaluronan binding protein involved in hyaluronan depolymerization (HYBID, KIAA1199) in the mouse central nervous system. Neuroscience 347, 1–10, doi:10.1016/j.neuroscience.2017.01.049 (2017). [PubMed: 28189611]
25. Zhang H et al. Identification of distinct nanoparticles and subsets of extracellular vesicles by asymmetric flow field-flow fractionation. Nat Cell Biol 20, 332–343, doi:10.1038/s41556-018-0040-4 (2018). [PubMed: 29459780]
26. Winkler F Hostile takeover: how tumours hijack pre-existing vascular environments to thrive. J Pathol 242, 267–272, doi:10.1002/path.4904 (2017). [PubMed: 28390068]
27. Fidler IJ The role of the organ microenvironment in brain metastasis. Semin Cancer Biol 21, 107–112, doi:10.1016/j.semcancer.2010.12.009 (2011). [PubMed: 21167939]
28. Arnold T & Betsholtz C The importance of microglia in the development of the vasculature in the central nervous system. Vasc Cell 5, 4, doi:10.1186/2045-824X-5-4 (2013). [PubMed: 23422217]
29. Tran QK, Ohashi K & Watanabe H Calcium signalling in endothelial cells. Cardiovasc Res 48, 13–22 (2000). [PubMed: 11033104]
30. Liebner S et al. Wnt/beta-catenin signaling controls development of the blood-brain barrier. J Cell Biol 183, 409–417, doi:10.1083/jcb.200806024 (2008). [PubMed: 18955553]
31. Shimizu H et al. Hyaluronan-Binding Protein Involved in Hyaluronan Depolymerization Is Up-Regulated and Involved in Hyaluronan Degradation in Human Osteoarthritic Cartilage. Am J Pathol 188, 2109–2119, doi:10.1016/j.ajpath.2018.05.012 (2018). [PubMed: 29935163]
32. Burri PH, Hlushchuk R & Djonov V Intussusceptive angiogenesis: its emergence, its characteristics, and its significance. Dev Dyn 231, 474–488, doi:10.1002/dvdy.20184 (2004). [PubMed: 15376313]
33. Dimova I et al. Inhibition of Notch signaling induces extensive intussusceptive neo-angiogenesis by recruitment of mononuclear cells. Angiogenesis 16, 921–937, doi:10.1007/s10456-013-9366-5 (2013). [PubMed: 23881168]
34. Giacomini A et al. Brain angioarchitecture and intussusceptive microvascular growth in a murine model of Krabbe disease. Angiogenesis 18, 499–510, doi:10.1007/s10456-015-9481-6 (2015). [PubMed: 26310512]
35. Doron H, Pukrop T & Erez N A Blazing Landscape: Neuroinflammation Shapes Brain Metastasis. Cancer Res 79, 423–436, doi:10.1158/0008-5472.CAN-18-1805 (2019). [PubMed: 30679177]

36. Tominaga N et al. Brain metastatic cancer cells release microRNA-181c-containing extracellular vesicles capable of destructing blood-brain barrier. Nat Commun 6, 6716, doi:10.1038/ncomms7716 (2015). [PubMed: 25828099]

37. van der Vos KE et al. Directly visualized glioblastoma-derived extracellular vesicles transfer RNA to microglia/macrophages in the brain. Neuro Oncol 18, 58–69, doi:10.1093/neuonc/nov244 (2016). [PubMed: 26433199]

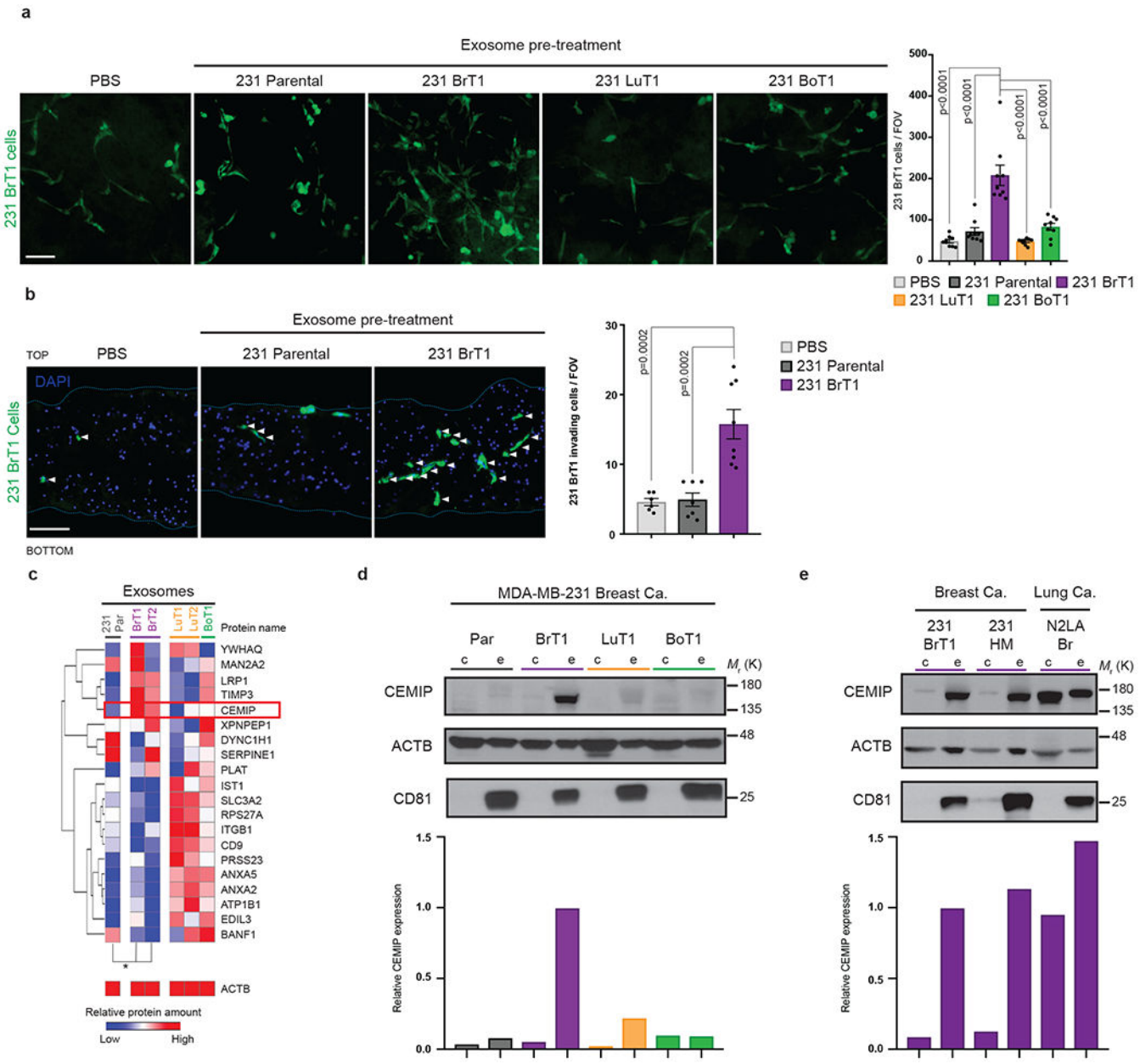

Figure 1 –. Exosomes from brain metastatic cells support brain metastatic colonization and are enriched in CEMIP protein.

a, Left, representative images of 231 BrT1-GFP^{+} cells growing on top of brain slices pre-treated with exosomes or PBS. Right, quantification of cancer cell number. **b**, Left, representative images of 231 BrT1-GFP^{+} cells invading brain slices pre-treated with exosomes or PBS. Brain slice sections were stained with DAPI (blue); dotted blue lines delineate the top and bottom limit of the brain slice. Right, quantification of invading cancer cell number. **c**, Heatmap of 20 differentially expressed exosomal proteins and β-Actin (ACTB) based on the quantitative mass spectrometry label-free quantification (LFQ) values (technical triplicates, *FDR - false discovery rate < 0.05 by ANOVA). Hierarchical clustering (one minus the sample Spearman's rank of correlation between observations) was

performed on protein expression levels. **d**, Top, CEMIP, ACTB (loading control), and CD81 (exosomal marker) immunoblot in cells and exosomes from organ-specific metastasis models. Bottom, densitometry quantification of CEMIP **e**, Top, CEMIP, ACTB (loading control), and CD81 (exosomal marker) immunoblot in cells and exosomes from human cancer cell brain metastasis models. Bottom, densitometry quantification of CEMIP. The number of cells per field of view (FOV) are averages ± SEM, from $n = 9$ individual brain slices (**a**), or $n = 6, 7, 8$ individual brain slices (**b**), scoring two fields per slice (**a**, **b**). Heatmap depicting differentially expressed proteins in BrT-derived exosomes displays average of three independent exosome sample replicates (**c**). Densitometry graphs show CEMIP expression normalized to CEMIP expression in BrT1 exosomes, and CEMIP expression was normalized to ACTB for each sample (**d** and **e**). A representative experiment of three (**a**, **b** and **e**) or four (**d**) independent biological replicates is shown. Scale bars, 100μm (**a**, **b**). Error bars depict mean ± standard error of the mean (SEM). *P* values were calculated by ANOVA (**a**, **b**). See Supplementary Figure 6 for unprocessed blots. See Supplementary Table 1 for statistics source data.

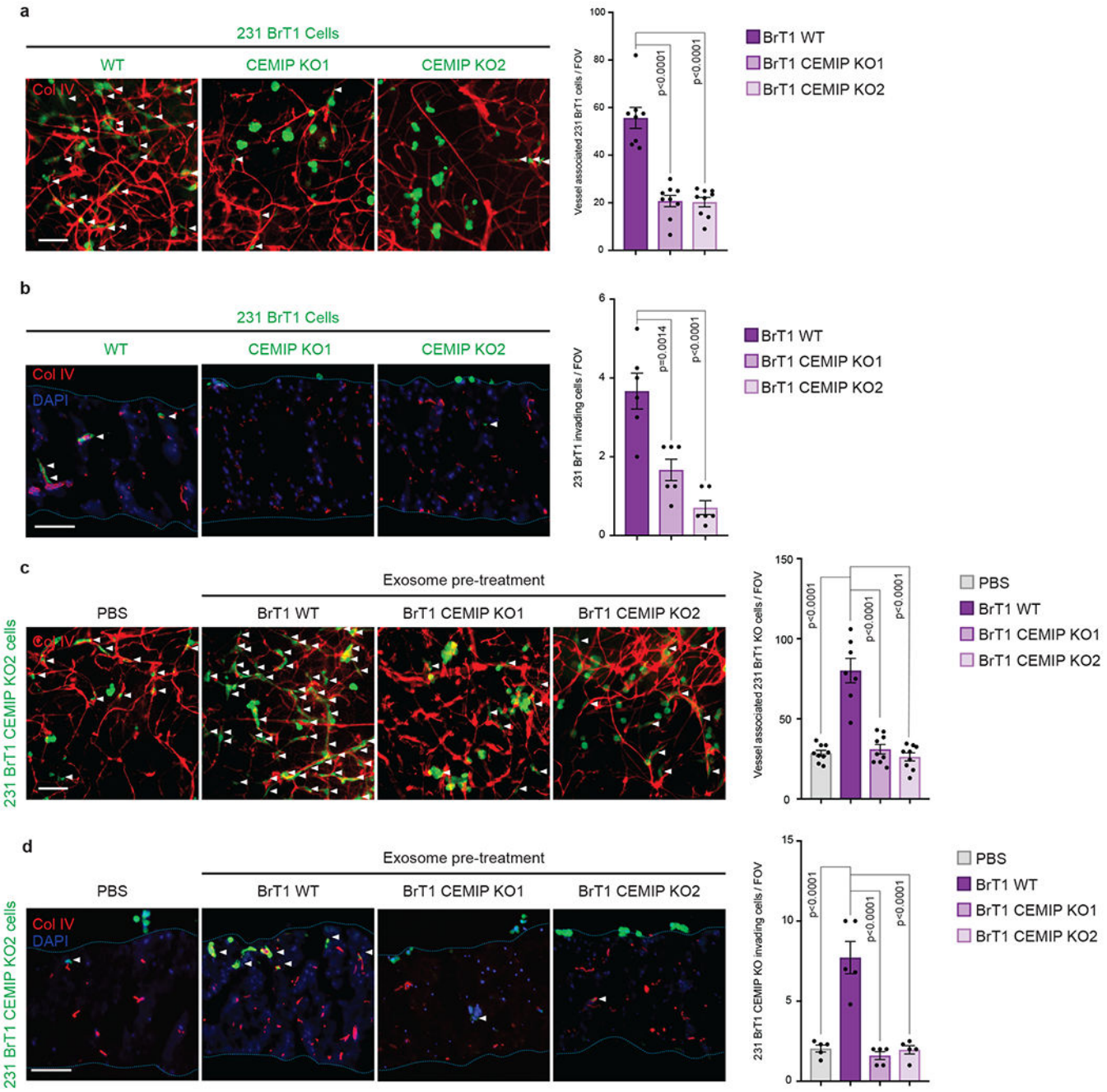

Figure 2 –. Exosomal CEMIP modulates the brain vascular niche to support vascular co-option and invasion.

a, Left, representative fluorescence microscopy images of vessel association of GFP-expressing BrT1 wild-type (WT, control cells with WT CEMIP expression) or GFP-expressing BrT1 CEMIP knockout (KO1 and KO2) cells growing on top of brain slices. Brain vasculature is shown by Col IV^{+} staining (red, all fluorescent images in Fig. 2a – 2d). Cells with spindle-like morphology and spread along vasculature (white arrows) were considered vessel-associated. Right, quantification of vessel-associated cancer cell number. **b**, Left, representative fluorescence microscopy images of BrT1 WT, BrT1 CEMIP-KO1,

and CEMIP-KO2 GFP$^+$ cells invading brain slices. Cancer cells were considered invasive when migrating inwards past the top cell layer of the brain slice (white arrows). Dotted blue lines delineate the top and bottom limits of the slice. Right, quantification of invading cancer cell number **c**, Left, representative fluorescence microscopy images of vessel association of BrT1 CEMIP-KO2 GFP$^+$ cells growing on top of brain slices pre-treated with exosomes or PBS. White arrows indicate vasculature-associated cancer cells. Right, quantification of vessel-associated cancer cell number. **d**, Left, representative fluorescence microscopy images of BrT1 CEMIP-KO2 GFP$^+$ cells invading (white arrows) brain slices pre-treated with exosomes or PBS. Dotted blue lines delineate the top and bottom limits of the brain slice. Right, quantification of invading cancer cell number. The number of cells per FOV are from $n = 8, 9, 9$ (**a**), $n = 6$ (**b**), $n = 9, 7, 9, 9$ (**c**), or $n = 5$ (**d**) individual brain slices, scoring two fields per slice. A representative experiment is shown from three (**a** - **d**) independent biological replicates. Brain slice sections are stained with DAPI, shown in blue (**b**, **d**). Scale bar, 100μm (**a** - **d**). Error bars depict mean ± SEM. *P* values were calculated by ANOVA (**a** - **d**). See Supplementary Table 1 for statistics source data.

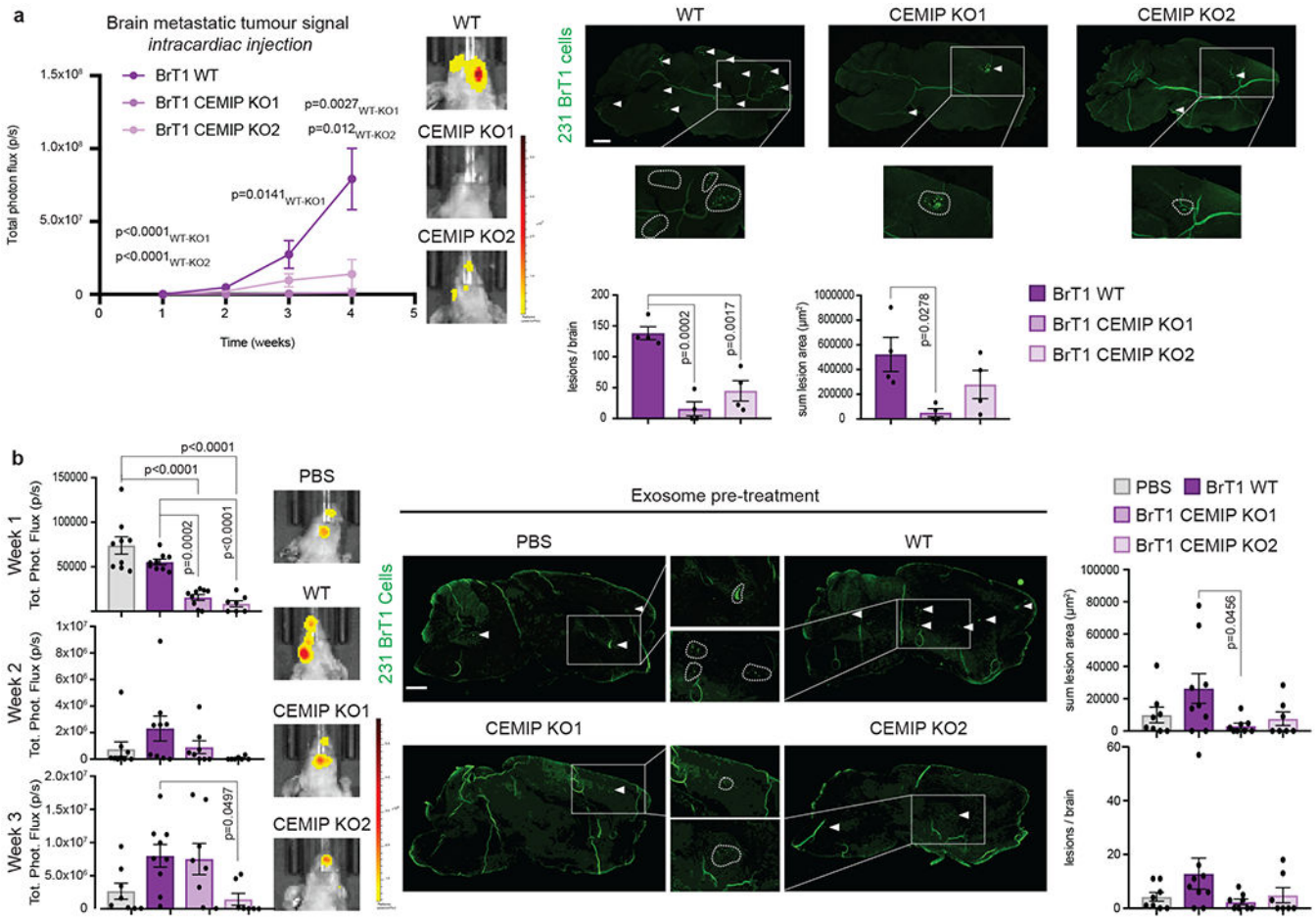

Figure 3 –. Exosomal CEMIP supports brain metastasis *in vivo*.

a, Quantification of brain metastasis in mice intracardiacally injected with BrT1 WT or CEMIP-KO cells. Left, cranial bioluminescence signal (Total photon flux – photons/ second (p/s)) in mice over 4 weeks post-intracardiac injection of GFP-labelled BrT1 WT or BrT1 CEMIP-KO luciferase-positive cells and representative IVIS image of brain signal at week 4. Right, representative immunofluorescence images of whole brain sagittal sections from mice with brain metastatic lesions after 4 weeks (green, white arrows). Quantification of the number of lesions per brain (left graph) and total brain metastatic lesion area (µm^2, right graph) is shown below the immunofluorescence images. The number of lesions and total metastatic area per brain represent averages ± SEM, scored from lesions in two sagittal brain sections from different brain areas per mouse, and n = 4, 5, 5 mice per group **b**, Quantification of brain metastasis in mice pre-educated with exosomes or PBS. Left, cranial bioluminescence signal (Total photon flux – photons/ second (p/s)) of mice educated for 3 weeks with exosomes or PBS, followed by intracardiac injection of GFP-labelled BrT1 luciferase-positive cells, and representative IVIS image of brain signals at week 3 post-cell injection. Enlarged inset, middle, representative images of whole brain sagittal sections from mice showing GFP+ brain metastases (green, white arrows) 3 weeks post-cell injection. Right, quantification of total brain metastatic lesion area (µm^2, upper graph) and number of lesions per brain (lower graph), representing averages ± SEM scored from lesions in two

sagittal brain sections representative of different brain areas per mouse, with n = 9, 9, 9, 7 mice per group. Scale bar, 1mm (**a**, **b**). Error bars depict mean ± SEM. P values were calculated by ANOVA (**a**, **b**). One representative experiment of two is shown (**a**, **b**). See Supplementary Table 1 for statistics source data.

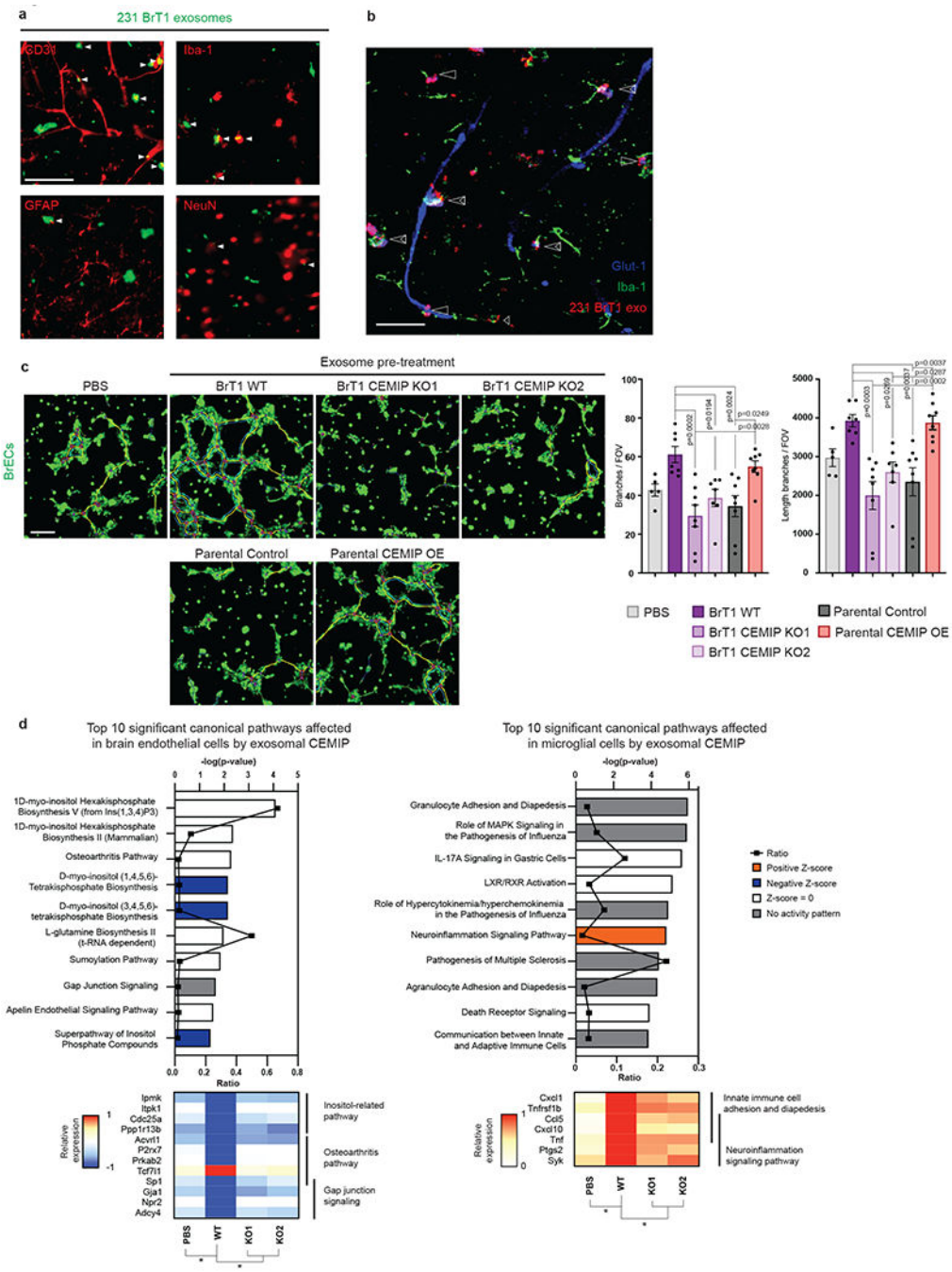

Figure 4 –. Exosomal CEMIP uptake by BrECs and microglia induces vascular remodeling and inflammation in the brain vascular niche.

a, Representative images of fluorescently-labelled 231 BrT1 exosomes (green) and brain endothelial cells (BrECs, $CD31^+$), microglia ($Iba1^+$), astrocytes ($GFAP^+$), or neurons ($NeuN^+$) (all in red). White arrows indicate co-localization of exosomes and the indicated cell type. **b**, Representative confocal microscopy image of $Glut1^+$ BrECs (blue, long arrows) and $Iba1^+$ microglia (green, short arrows) interacting with fluorescently-labelled BrT1 exosomes (red). Double arrows depict joint interaction of BrECs and microglia with exosomes. **c**, Left,

representative images of calcein AM-loaded BrEC vascular networks (green) formed *in vitro* upon pre-treatment with exosomes or PBS. Vascular tree general topology is depicted by identification of the tree's master junctions (red) and master segments (yellow). Right, quantification of vascular network branch number (left graph) and length (right graph). **d**, Top, pathways affected by exosomal CEMIP in BrECs (left) and microglia (right) isolated from exosome-treated brain slices. Z-score indicates activation (orange) or inhibition (blue), and ratio indicates number of genes from the CEMIP list that map to a pathway divided by the total number of genes that map to that same pathway. Associated p-value of the Fisher's exact test is displayed in black. Bottom, heatmap of differentially expressed genes involved in selected pathways. The number and length of branches per FOV are averages ± SEM, from n = 5, 7, 8, 7, 8, 8 individual μ-slide wells (**c**), scoring a representative field per well. One of three independent biological replicates is shown for **a, b, c**. The average of three independent biological replicates is displayed in (**d**). Scale bars, 100μm (**a**, **c**) and 50μm (**b**). Error bars depict mean ± SEM. P values were calculated by ANOVA (**c**) and Fisher's exact test (chart) or two-sided Student's t-test (heatmap) (**d**). See Supplementary Table 1 for statistics source data.

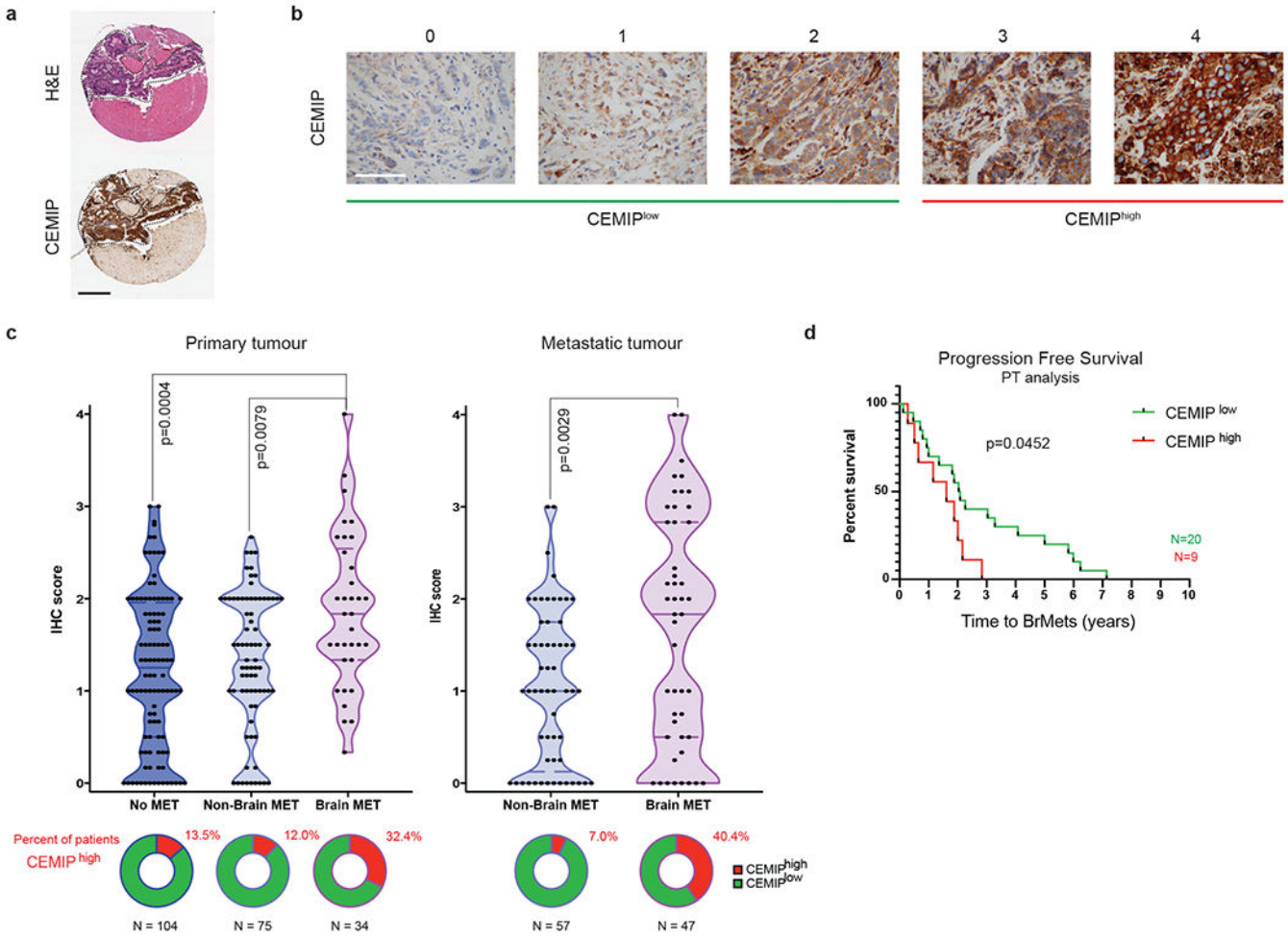

Figure 5 –. CEMIP is a prognostic biomarker of brain metastasis in patients.

a, Representative image of a lung cancer brain metastatic tumour patient sample analyzed by H&E (top) and CEMIP immunohistochemistry (bottom). The metastatic tumor is outlined by the black dashed line. **b**, Representative immunohistochemistry images illustrating CEMIP expression for each scoring category in patient tumour samples. Samples with no (0) or low (1 and 2) CEMIP staining were considered CEMIP^{low} (green). Samples displaying high expression (3 and 4) were considered CEMIP^{high} (red). **c**, Top, quantification of CEMIP expression by immunohistochemistry in primary tumour (left) and metastatic tumour (right) from patients with or without brain metastasis. Bottom, percentage of CEMIP^{high} cases and information on total number of samples evaluated in each group. PT (Minimum: 0.00, 0.00, 0.33; Maximum: 3.00, 2.67, 4.00; and Median: 1.25, 1.33, 1.83), and MET (Minimum: 0, 0; Maximum: 3, 4; and Median: 1.00, 1.83). **d,** Progression-free survival Kaplan-Meier curve for brain metastasis patients depicting time to brain metastasis based on primary tumour CEMIP expression, low (green) or high expression (red). Scale bars, 50μm (**a**), and 300μm (**b**). Human data consists of n=317 total unique tumour samples (213 primary and 104 metastatic) from 278 breast and lung cancer patients (**a** - **c**). Immunohistochemistry score represents the average intensity in tumour cores analyzed (1 – 3 per sample) on a scale from 0 to 4 (**b**). Dashed line across violin plots depicts quartiles and

full line depicts median (**c**). *P* values were calculated by ANOVA and two-sided Student's t-test (**c**), or Log-rank (Mantel-Cox) test (**d**). See Supplementary Table 1 for statistics source data.